

Effect of microstructure evolution on the creep properties of a polycrystalline 316H austenitic stainless steel

Jianan Hu^{a,b*}, Graham Green^{c,d,1}, Simon Hogg^c, Rebecca Higginson^c, Alan C.F. Cocks^a

^a*Department of Engineering Science, University of Oxford, OX1 3PJ, UK*

^b*Sente Software Ltd, Surrey Technology Centre, Guildford, GU2 7YG, UK*

^c*Department of Materials, Loughborough University, LE11 3TU, UK*

^d*Rolls Royce plc, Derby, DE24 7XX, UK*

ABSTRACT

Creep deformation and failure is one of the most critical life limiting factors of structural components used at elevated temperatures, such as in nuclear power plants. Understanding of the mechanisms of creep in nuclear power plant steels, such as Type 316H austenitic stainless steels, is still incomplete. It has been observed that long-term creep curves of initially solution-treated (ST) 316H stainless steels exhibit multiple secondary stages at the operational temperature and stress range. This paper probes the internal mechanisms for this complex phenomenon by correlating and quantifying the evolution of microstructural state (dislocations, precipitation and solid solution elements) and its mechanistic influence on the material's creep properties. This is examined for the first time by a multi-scale self-consistent crystal plasticity framework combined with a simple classical phase transformation model and thermal solute strengthening model. The novel integrated model is capable of describing a broad range of physical processes, including dislocation multiplication (hardening) and climb-controlled recovery, precipitation nucleation, growth and coarsening (Ostwald Ripening) and thermal solute dragging. The mechanisms responsible for the observed multiple secondary stages in the creep curves of initially solution-treated 316H stainless steels are explained through the strengthening and softening effects associated with these processes.

Keywords: Microstructure evolution; Creep property; Phase transformation; Stainless steel.

* Corresponding author: *E-mail address:* jianan.hu@sentesoftware.co.uk

¹ Current *E-mail address:* graham.green@rolls-royce.com

1. Introduction

Creep deformation and failure has been regarded as one of the most critical life limiting factors of engineering components used at elevated temperatures, such as in nuclear power plants [1, 2]. Austenitic stainless steels, typically Type 316H, are extensively used in nuclear components due to their high resistance to corrosion and good creep properties. A comprehensive understanding of the internal mechanisms of creep in these materials during complex thermo-mechanical loading conditions, either globally or locally within the components, is crucial to life assessment and prediction in order to avoid unexpected failure of critical components, which could cause closure of the whole nuclear power plant [2, 3].

Constitutive models of creep behaviour at elevated temperatures have been investigated for decades. A variety of fundamental analytical models can be traced back to the traditional Norton and Arrhenius law for secondary creep [4], time or strain hardening laws for primary creep [5], and continuum damage mechanics models for tertiary creep [6]. The capability of these models has been discussed and developed extensively in the scientific literature regarding the interpretation of uniaxial creep data, e.g. [2, 6-8]. However, these models are either empirical or phenomenological, and they are not able to fully explain the underlying physics of all the observed phenomena [2, 3]. One such complex phenomenon is “multiple secondary stages or multiple minimum creep rates” observed in long-term creep tests at some intermediate stresses and/or temperatures of initially solution-treated (ST) Type 316H austenitic stainless steels [9-12]. Figure 1 compares the entire creep rate vs. time curves of ST 316H obtained at 600°C and 650°C, which depicts how the creep rate evolves from primary to secondary and tertiary stage at each stress. At 650°C between 83 MPa and 108 MPa in Fig. 1(b), two secondary stages can be clearly observed, as reflected from the two troughs at each stress representing two constant minimum creep rates. Figure 2 compares the entire creep rate vs. time curves of two batches of ST 316H with slightly different chemical compositions and prior thermal histories at 600°C and 650°C tested at the same stresses. It shows that the “multiple secondary stages” may vary with the change in chemical composition, demonstrating the intrinsic complexity of the internal mechanisms.

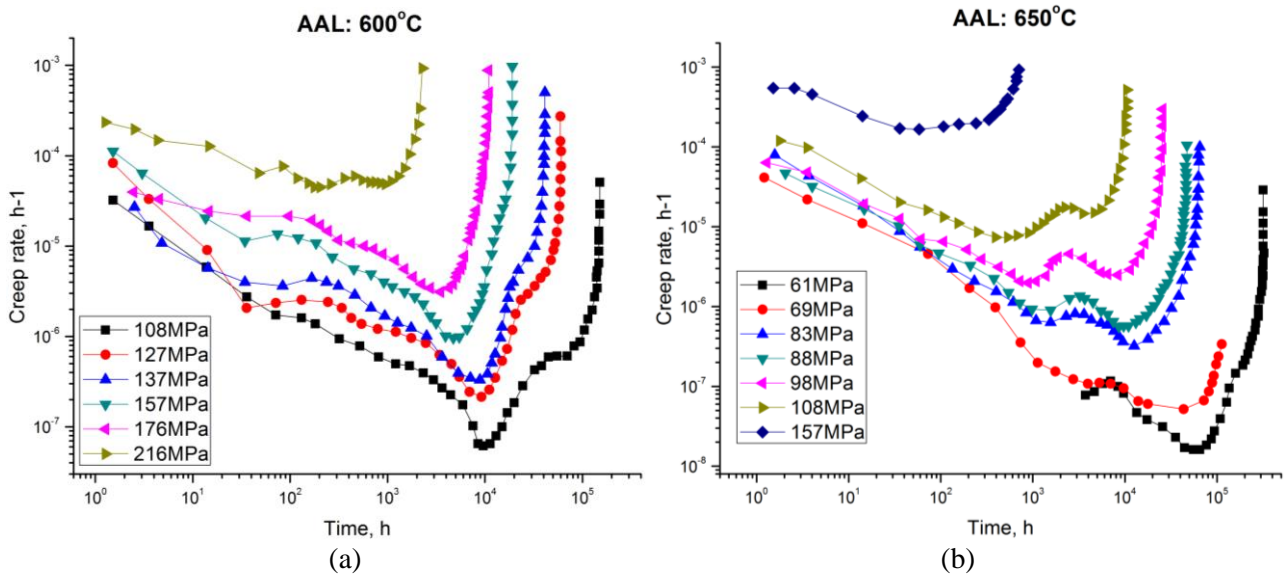


Figure 1. Creep rate vs time curves of initially solution-treated (ST) Type 316H stainless steels at (a) 600°C and (b) 650°C. AAL is the reference code of the specimen and data are obtained from [10]

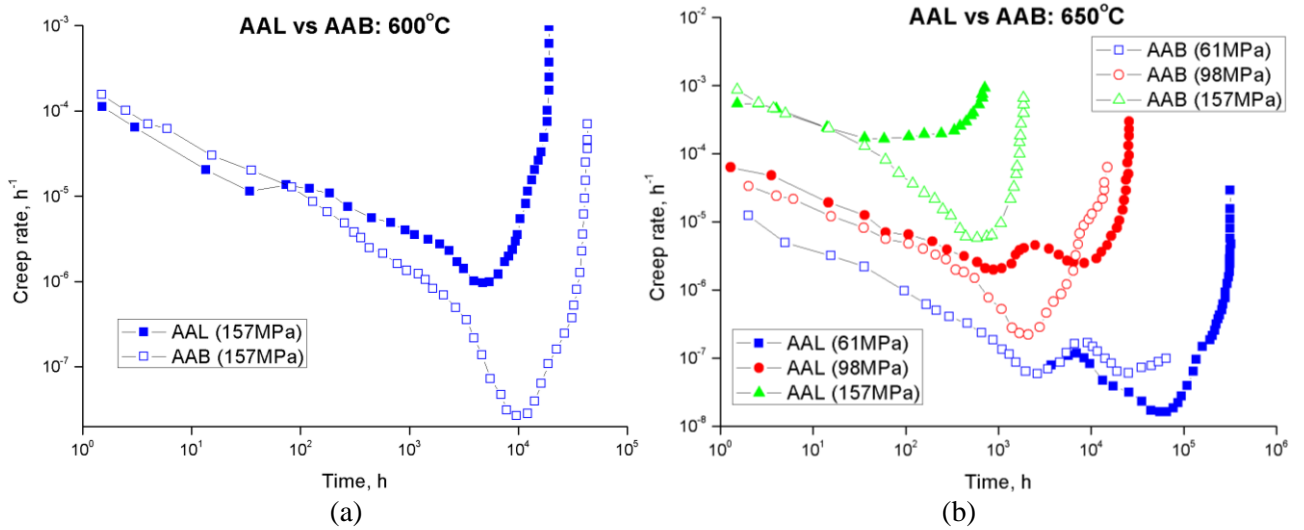


Figure 2. Comparison of creep rate vs time curves of two initially solution-treated (ST) Type 316H stainless steel specimens (with slightly different chemical compositions) at same stresses at (a) 600°C and (b) 650°C. AAL and AAB are the reference code of the specimens and data are obtained from [10]

The occurrence and complexity of the “multiple secondary stages” demonstrate that

- (1) There is an evident correlation between the microstructural state and a material’s creep properties, as different precipitates and phases can form out of the initially supersaturated alloys during creep, which then changes the composition of the matrix phase.
- (2) Accelerated tests conducted either beyond the operation temperature or applied stress range may not reproduce the identical microstructural state as obtained during long-term exposure at the operation condition, as there are a range of kinetic processes that can change as the test conditions and environment are changed. Deformation mechanisms may also change depending on the microstructural state of the material [13, 14].

These observations suggest that, for realistic long-term life predictions, structural integrity assessments require the development of simple mechanistically motivated constitutive models with foundations in physics that can deal successfully with different thermo-mechanical loading and material conditions. Any robust physical model of this type may require: 1) physical state variables that can describe the material’s mechanistic internal state [15]; and 2) microstructural models that can successfully capture the detailed microstructure evolution process and its mechanistic relationship with the material’s creep behaviour.

The crystal plasticity framework is a suitable candidate for the development of physical models, since it describes the material’s inelastic deformation as a result of dislocation motion on elementary slip systems [16]. Typical examples of models of this type can be found in [17-19], which have been used and validated in a number of studies of elasto-plastic deformation. It has also been applied successfully to the study of creep and relaxation behaviour [20]. However, one common problem with the conventional approach is the simplified hardening law generally employed on each slip system, with the adoption of either empirical or phenomenological laws. A mechanistic link between the evolution of different microstructural elements and a material’s creep behaviour is still lacking. In our previous work, a multi-scale self-consistent crystal plasticity model has been proposed [16, 21], where the roles of different microstructural elements (typically dislocations, precipitates and solid solution elements) on a material’s mechanical behaviour at room temperature has been established. A thermodynamic approach has been further developed to physically model dislocation climb-controlled recovery and its effect on creep [22]. The model has been validated on initially ex-service plus laboratory aged Type 316H stainless steels subject to plasticity or short-term creep [16, 21, 22], in which the microstructural state has been regarded as stable without any further evolution of precipitates or of elements in solid solution. Under these conditions the material does not exhibit “multiple secondary stages”.

This study aims to: extend our previous work by incorporating the evolution of precipitates and solid solution elements into the model; probe the microstructure-creep property relationship; and explore to what extent the extended model can capture the complex phenomenon of “multiple secondary stages” in initially solution-treated (ST) 316H stainless steels. Here, a classical physically based diffusion-controlled phase transformation model [23-25] is used for the first time to describe the precipitation or phase transformation process in 316H stainless steels. It is also for the first time to take into account the real-time effect of microstructure evolution on the creep property for this material.

2. Framework of the self-consistent crystal plasticity model

The physical self-consistent framework used in this paper is a multi-scale framework that is developed from the length-scale of elementary slip activity through to the individual grain or crystal level and then to the continuum level. Here we first briefly describe the key principles of different parts of model and then focus on the new features, i.e. the kinetics and phase transformation model. For details of the self-consistent framework, one can refer to [3, 16, 21, 22].

The continuum model establishes the relationship between the elastic-plastic response of individual grains and that of the polycrystalline aggregate based on a fundamental inclusion model [26, 27]. Due to the variation in orientation, grains exhibit different responses subject to a global remote load and thus yield progressively as the material is loaded. The localized plasticity induced mismatch between plastically deformed grains and the surrounding matrix can generate grain-scale residual stress [28, 29], which combines with the applied stress to determine the stress-strain state in each grain.

The crystal plasticity framework describes and calculates the plastic strain (or strain rate) of individual grains as a collection of the resolved shear strains (or shear strain rates) on all the active slip systems [30, 31]. The deformation kinetics on a given slip system is described by a thermally activated glide rule according to [4, 22]:

$$\dot{\gamma} = \dot{\gamma}_0 \exp \left(-\frac{\Delta F_0}{kT} \left(1 - \left| \frac{\tau + \tau_{in}}{(1 + F_{sol}) \tau_{cr}} \right|^{3/4} \right)^{4/3} \right) \text{sgn}(\tau) \quad (1)$$

where τ and τ_{cr} are respectively the resolved shear stress (RSS) and critical resolved shear strength (CRSS) on a given slip system, with the latter associated with three major microstructural elements or obstacles that a moving dislocation can encounter on its slip plane (forest dislocation junctions, intragranular precipitates and solute atoms) [16, 21]; τ_{in} is a micro-scale internal stress associated with dislocation loops generated when dislocations bypass precipitates (details in [21]); $\dot{\gamma}_0$ is a reference shear strain rate, which is taken to be 1/s [3, 16, 21]; k is Boltzmann’s constant; T is absolute temperature; $\Delta F_0 = \alpha_0 G_0 b^3$ (α_0 : an average strength constant for all obstacles; G_0 : shear modulus at 0 K; b : magnitude of Burgers vector) is an approximate average total activation energy required to overcome all types of obstacles [3, 4].

F_{sol} is a new phenomenological feature added to our previous model [22], describing the enhancement of CRSS by some specific mobile solute atoms in the matrix, which, with enhanced mobility at elevated temperatures, can readily diffuse and form complexes, atmospheres or clusters surrounding and being dragged along with the gliding and climbing dislocations [8]. Such a kinetic process is often referred to as a *solute drag mechanism* where the motion of dislocations is impeded and limited by the diffusivity of certain species of mobile solutes. F_{sol} has been considered as history-independent, i.e. it is a function only of the instantaneous strain rate and temperature [8, 32]. Here a simplified version of F_{sol} is incorporated in our framework, retaining the essential physics of the solute drag process [32]. Following Henshall and Miller [32] we write:

$$F_{sol} = A c_s \exp \left[- \left(\frac{\log(\xi) - \log(\xi_{max})}{B} \right)^2 \right] \quad \text{such that} \quad \xi = \frac{|\dot{\gamma}|}{\Theta} = |\dot{\gamma}| \exp \left(\frac{Q_{sol}}{RT} \right) \quad (2)$$

where A is a temperature-dependent fitting constant, B is a temperature and strain rate independent fitting constant. c_s is the current concentration of the species in the solute complexes. $\Theta = \exp(-Q_{sol}/RT)$ where R is the universal gas constant and Q_{sol} is the activation energy for the process controlling solute drag - we assume that this is given by the activation energy for dislocation core diffusion for the dominant element responsible for the drag process. ξ_{max} is a material constant related to the critical shear strain rate and temperature at which solutes in the clusters and dislocations move at the same velocity and thus the solute drag effect achieves its maximum effect. Solute drag would attenuate when solute clusters disappear by precipitation ($c_s \approx 0$, as in our previous work of ex-serviced plus laboratory aged materials), or the shear strain rate is relatively slow ($\dot{\gamma} < \dot{\gamma}_{max}$, solute clusters diffuse much faster) or fast ($\dot{\gamma} > \dot{\gamma}_{max}$, dislocations glide or climb much faster).

3. Microstructure model: structure-property relationship

The CRSS in Eq. (1) physically characterises the internal resistance for dislocations to overcome and bypass different types of randomly distributed obstacles on individual slip planes [16]. Here the obstacles originate from three major microstructural elements: forest dislocation junctions (intersections or pinning points of dislocation segments from other slip planes [16, 33]), precipitates (assumed to be spherical strong particles that dislocations can only bypass through the Orowan bypass mechanism [34]) and solute atoms (isolated elements in solution, associated with athermal solute strengthening [16], not to be confused with the thermal solute drag described above from gathered solute clusters). Note that thermal activation may trigger an alternative precipitate bypassing mechanism, in which with enhanced mobility, dislocations held at precipitates can potentially climb and bypass particles, thus resulting in a reduced strengthening effect compared with the Orowan bypass mechanism. While this complexity has been discussed in [3, 14], it is not modelled in this work, but will be discussed later in the interpretation of results.

The contributions of these different processes to the CRSS can be expressed by the following law [35, 36]

$$\tau_{cr} = \sqrt{\tau_d^2 + \tau_p^2} + \tau_s = \sqrt{\left(\frac{\alpha_d G b}{L_d} \right)^2 + \left(\frac{\alpha_p G b}{L_p} \right)^2} + \frac{\alpha_s G b}{L_s} \quad (3)$$

where G is the temperature-dependent shear modulus [4], α is a dimensionless constant describing the obstacle strength, with the subscripts “ d , p , s ” representing dislocation junctions, precipitates and solute atoms respectively. L is the physical microstructural state variable, representing the mean spacing between each type of obstacles, which is inversely proportional to the square root of the number density. Evolution of the three strengthening terms (τ_d, τ_p, τ_s) can be characterised by the change of the state variable L , as a consequence of the evolution of microstructure when the material is subject to load and/or exposure at elevated temperatures.

3.1 Evolution of L_d

The length scale L_d for forest dislocations ($L_d = N_d^{-1/2}$, N_d : number density of junctions) evolves by the glide-controlled multiplication and climb-controlled recovery of the dislocation network. The former involves self- and latent hardening by the interaction of dislocations from different slip planes [16, 21, 37], while the latter requires thermally activated dislocation core or pipe diffusion that leads

to the growth of long dislocation segments at the expense of shorter ones [22]. Competition between the hardening and recovery processes is the main deformation mechanism for creep and the secondary stage is reached when the two processes are dynamically balanced. Detailed derivations of this part of models can be found in the above references and are not considered further here.

3.2 Evolution of L_p

The length scale L_p for precipitates evolves by the phase transformation process at elevated temperature, which is another new feature added to our previous model, as illustrated in detail in this section. Note, only the intragranular precipitates are to be considered here as responsible for the strengthening by the Orowan bypass mechanism. For randomly distributed spherical precipitates on each slip plane, L_p is expressed as [38, 39].

$$L_p = r_p \sqrt{\frac{2\pi}{3f_v}} \quad (4)$$

where f_v and r_p are the volume fraction and mean radius of all the intragranular precipitates. Transformation of precipitates leads to the evolution of f_v and r_p , which consists of three sub-processes, nucleation, growth and coarsening, with the first two processes described by an extended Johnson-Mehl-Avrami-Kolmogorov (JMAK) model taking into account non-constant nucleation and growth rates [24, 25], and the last process is described by the Lifshitz-Slyozov-Wagner (LSW) Ostwald Ripening model [40].

3.2.1 Nucleation

In the JMAK theory, during the nucleation and growth processes, the change of volume fraction (Δf_v) of a given precipitate phase during a time interval Δt can be expressed as

$$\Delta f_v = (1 - f_v) \dot{N}_v \Delta t \cdot \frac{4\pi}{3} (\dot{r}_p \Delta t)^3 \quad (5)$$

where \dot{N}_v is the nucleation rate per unit volume and \dot{r}_p is the rate of increase of the mean radius r_p of the precipitates. If n precipitate phases transform simultaneously, Eq. (5) changes to

$$\Delta f_{vi} = \left(1 - \sum_{k=1}^n f_{vk} \right) \dot{N}_{vi} \Delta t \cdot \frac{4\pi}{3} (\dot{r}_{pi} \Delta t)^3 \quad (6)$$

where the subscript “ i ” denotes the corresponding quantity for the i th phase. \dot{N}_v can be calculated using the classical nucleation theory [41]

$$\dot{N}_v = N_0 Z \beta \exp \left(-\frac{G^*}{kT} \right) \quad (7)$$

where N_0 is the number density of potential nucleation sites per unit volume, Z is the Zeldovich factor, representing the probability that a nucleus of critical size determined by the magnitude of the energy barrier G^* will continue to grow to form the new phase and not dissolve. β is the condensation rate of atoms in a particle with critical radius, or the rate at which molecules attach to the nucleus causing it to grow. The product of Z and β is given as [24, 25, 42]:

$$Z\beta = \frac{2v_m D^r c^r}{a_m^4} \sqrt{\frac{\chi}{kT}} \quad (8)$$

where a_m is the lattice parameter of the parent phase, v_m is the molecular volume of the precipitate phase, χ is interfacial energy, D^r and c^r are the diffusivity and concentration of the rate-controlling element in the matrix for a given precipitate phase. The diffusivity is expressed in the form $D = D_0 \exp(-Q_0/RT)$, where D_0 is the pre-exponential and Q_0 is the activation energy. In Eq. (7), $G^* = 16\pi\chi^3/3G_v^2$ is the activation energy for nucleation where G_v is the chemical driving force for precipitation [24, 25]

$$G_v = -\frac{kT}{v_m} \ln\left(\frac{c}{c_{eq}}\right) \quad (9)$$

where c and c_{eq} are respectively the current and equilibrium solute concentration in the matrix regarding the precipitate composition. Note for compound phases, these concentrations are the product of all the components.

3.2.2 Growth

A diffusion-controlled Zener growth law [43] is used to describe the effective growth rate of a given precipitate phase

$$\left(\dot{r}_p\right)_{grow} = \frac{D^r}{r_p} \cdot \frac{c^r - c_{eq}^r}{c_p^r - c_{eq}^r} + \frac{\dot{N}_v}{N_v} (r_c - r_p) \quad (10)$$

where the first term refers to the evolution of mean radius r_p by pure growth as a simplified linear function of the concentration gradient of the rate-controlling element (see Fig. 3, c_p is the solute concentration in the precipitate phase), and the second term refers to the nucleation of new nuclei with the critical size $r_c = -2\chi/G_v$ in the existing population [24, 25]. As the precipitates grow, the solute concentration in the matrix decreases [23], which reduces the subsequent nucleation rate (Eq. 7) and growth rate (Eq. 10).

$$c^r = \frac{c_0^r - f_v c_p^r}{1 - f_v} \quad (11)$$

where c_0^r is the initial concentration.

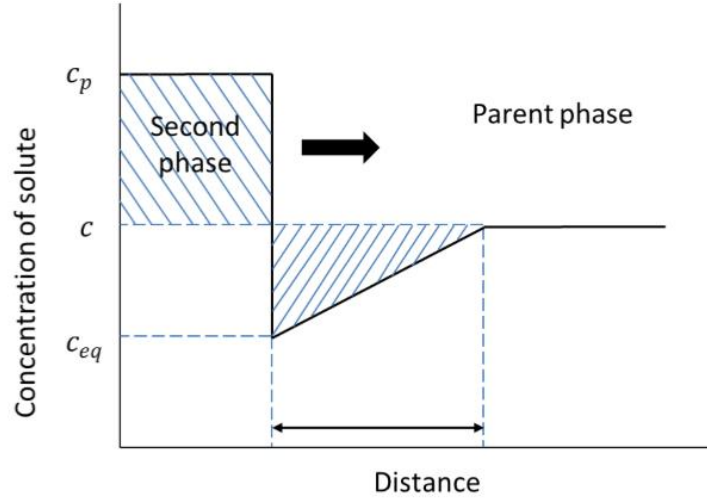


Figure 3. The constant solute concentration approximation profile after Zener [43] .

3.2.3 Coarsening

Nucleation ceases when the equilibrium solute concentration is achieved in the matrix ($c^r = c_{eq}^r$ in Eq. 10). Afterwards the precipitates coarsen (r_p increases), with large particles growing at the expense of smaller ones (Ostwald Ripening, Fig. 4), but the volume fraction remains unchanged [40]. According to the classical LSW theory [44], after a time t

$$r_p^3 = r_0^3 + Kt \quad \rightarrow \quad (\dot{r}_p)_{coars} = \frac{K}{3r_p^2} \quad (12)$$

where r_0 is the mean radius at the onset of coarsening and $K = 8\chi V_m^2 D^r c^r / 9RT$ is the coarsening rate parameter ($V_m = 6.02 \times 10^{23} v_m$ is the molar volume). In general, the nucleation and growth processes lead to strengthening while the coarsening process results in softening.

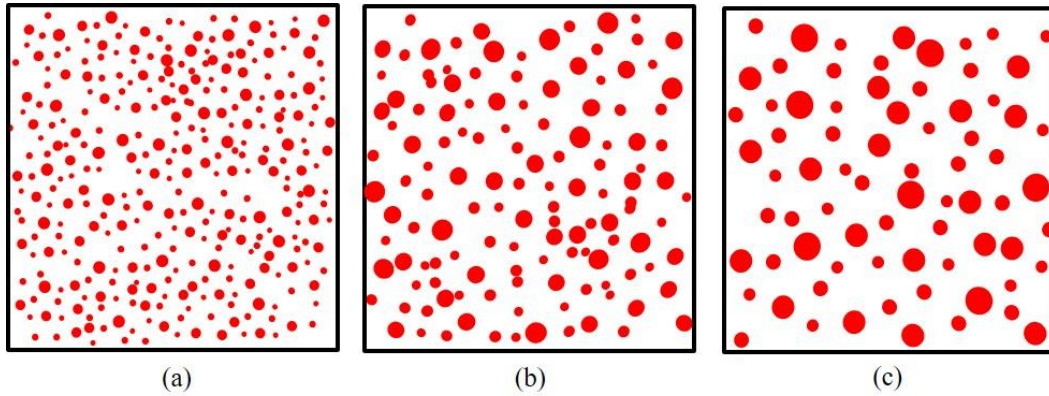


Figure 4. A schematic diagram of particle coarsening, or Ostwald-Ripening process with the passage of time. (a) Precipitation in the supersaturated solid solution. (b) and (c) The large particles grow while the smaller ones shrink

3.2.4 Effect of creep stress on precipitation

The process of phase transformation can be further promoted if the material is subjected to creep loading [12, 25, 45-47]. The effect of superimposed plasticity/creep on phase transformation can be divided into the following two potential aspects [25, 45, 46]:

- 1) Dislocations generated during inelastic deformation provide more energetically favourable nucleation sites and as a consequence the nucleation barrier or Gibbs free energy is reduced;
- 2) Dislocations act as short-circuit diffusion paths, and the exchange of solute between precipitates can occur by pipe diffusion through dislocation cores, which can then accelerate both growth and coarsening processes.

Despite these qualitative trends, to date, no simple models of the type employed here have been proposed or developed that can fully capture the effect of creep on the kinetics of phase transformation. Here a simple extension is employed to retain the basic physics. For aspect 1), an empirical scale factor w ($w \leq 1$) is used to modify the Gibbs free energy in Eq. (7), assuming that the heterogeneous nucleation barrier is proportional to the homogeneous one [46]

$$G^{*'} = wG^* \quad (13)$$

We do not further consider the influence on the nucleation site (N_0) since the rate dependence of the exponential is much larger than the pre-exponential in Eq. (7). For aspect 2), the effective diffusivity D^r is modified to combine bulk diffusivity D_L^r and pipe diffusivity D_p^r [4, 48]

$$D^r = D_L^r + a_c \rho D_p^r \quad (14)$$

Here $a_c \approx 2b^2$ is the area of the dislocation core, ρ is total dislocation density ($\rho \approx 1/L_d^2$).

3.3 Evolution of L_s and F_{sol}

Finally, L_s in Eq. (3) can increase by depletion of solute atoms in the matrix as a result of precipitation, as characterised by Eq. (11). As a consequence, the athermal solute strengthening (τ_s) attenuates [49, 50]. Further, the thermal solute drag effect (F_{sol} in Eq. 2) is also weakened if the elements in the solute clusters are depleted by precipitation. The concentration of the different elements in solution can be determined directly from the precipitate model described above. We discuss this further below when we analyse the response of a particular alloy.

4. Validation and evaluation of the model

Our previous work [16, 21, 22] has focused on 316H stainless steels with an initial condition determined by service exposure plus laboratory ageing, originally extracted by EDF Energy from Generation II nuclear power plant in the UK. In these specimens, a considerable population of both intergranular and intragranular precipitates existed [51]. Thus in the high temperature short-term creep simulations of the material [22], the phase transformation and the effect on thermal solute drag due to depletion by the existing precipitates have been ignored. In this section, we focus on long-term exposure to thermomechanical treatment of initially solution-treated (ST) thermodynamically unstable 316H (chemical composition shown in Table 1, which is the same as the AAL reference material used in the experiments reported in Fig. 1). We present a range of evaluations of the new features in the model to evaluate how they can capture the complex processes that determine the evolution of microstructure and how this influences the material's creep response.

Table 1. Chemical composition (wt.%) of Type 316H stainless steel

C	Si	Mn	P	S	Cr	Mo	Ni	Cu	N	Fe
0.07	0.61	1.65	0.025	0.007	16.6	2.33	13.6	0.26	0.025	Bal.

4.1 Evaluation of phase transformation during thermal ageing

In this section we evaluate the evolution of precipitate phases during pure thermal ageing in the absence of creep, using the extended JMAK phase transformation model described above. The time-temperature-precipitation (TTP) diagram for 316H stainless steel is shown in Fig. 5 [12], which demonstrates the major precipitate phases that can form during thermal ageing, which is similar to that reported elsewhere [45]. The multiple “C-curves” clearly identify the sequence of transformation and the “beginning of nucleation” of each phase. However, care needs to be taken in interpreting these curves as giving the true “beginning of nucleation” of each phase, since it roughly refers to the time when a given phase becomes experimentally observable and measurable, thus it is dependent on the experimental technique employed.

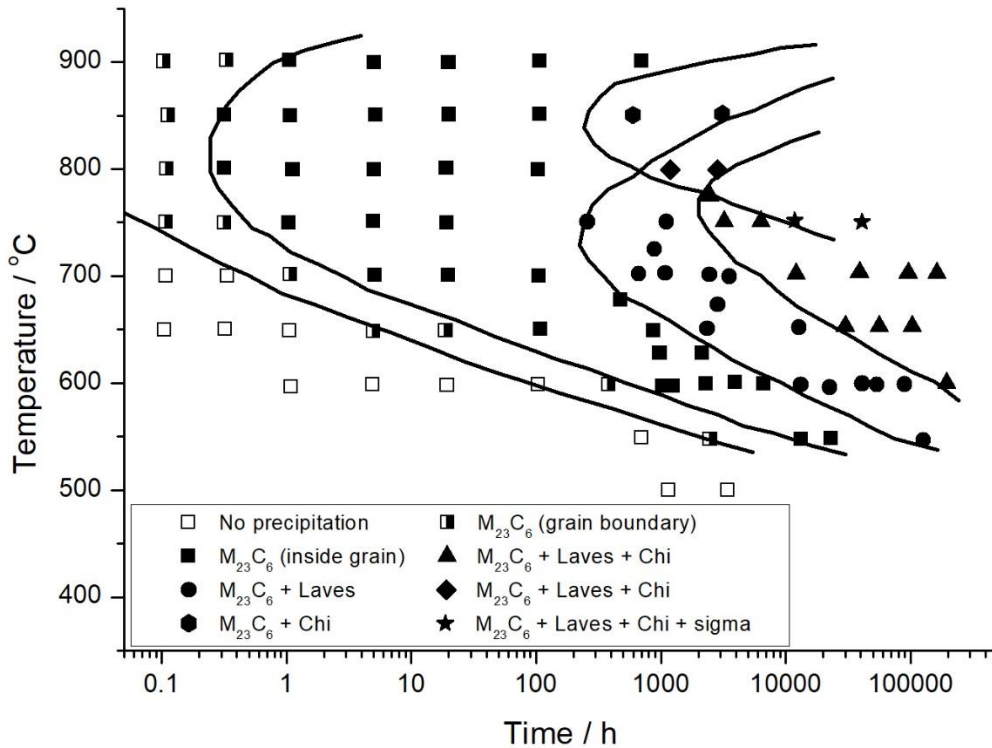


Figure 5. Time-temperature-precipitation (TTP) diagram of Type 316H stainless steels [12]. M in $M_{23}C_6$ carbides refers to metallic elements.

Taking into account the practical operating condition and life expectation of nuclear power plants in the UK, we focus on the temperature range 500°C~650°C, and limit our consideration to only two phases, respectively carbides and the intermetallic Laves phase, with the former reported to occur both along grain boundaries and inside grains while the latter mainly occurs within the grains. The chemical compositions of the two phases are simplified to be $Cr_{23}C_6$ (carbide) and Fe_2Mo (Laves), while the competition of other minor metallic elements between these two phases is considered empirically (to be shown later). As our main interest is the intragranular precipitates that can interact and retard dislocation motion inside the grains, a further assumption is made such that the initial state of the material already contains saturated intergranular $Cr_{23}C_6$ carbides with a constant volume fraction of 0.8% based on the experimental findings in [52].

4.1.1 Computational scheme and parameters

At the beginning of the simulation, no intragranular precipitates are present. The initial composition in the matrix is calculated taking into account the depleted solute elements due to the

aforementioned presence of the 0.8% volume fraction of intergranular $Cr_{23}C_6$ carbides. At each time step Δt , both intragranular carbides and Laves phase are allowed to transform simultaneously, with the number of newly formed particles of each phase ΔN_v per unit volume calculated by Eq. (7) and the mean size of all the existing intra-particles r_p of each phase calculated by Eq. (10). Then the increase of volume fraction of each phase Δf is updated by Eq. (6). Further, the solute concentration in the matrix is updated by Eq. (11), only for the controlling elements of each phase (Cr and C in carbides, Mo in Laves). Note that for carbides, growth is controlled by diffusion of Cr but saturation is controlled by the amount of C [53, 54]. The change in concentration further changes the nucleation and growth rate in the subsequent time steps. For each phase, this process is repeated until the concentration of the controlling element in the matrix reaches the equilibrium value, after which nucleation ceases and coarsening starts - the mean size is then updated using Eq. (12).

Values of the parameters used in this simulation are shown in Table 2. Seven parameters (nucleation site density N_0 , interfacial energy χ and molar volume V_m of carbide and Laves phase, and a coarsening reduction factor C_f for carbide) are selected to provide the best fit to the available data [12], as shown in Fig. 6. χ and V_m are adjusted based on the values estimated by [55-57]. The coarsening reduction factor C_f is used to reduce the coarsening rate of carbides, based on the fact that the formation of Laves phase can deplete some Cr in the matrix as some minor Laves phase has the chemical composition Fe_2Cr [12], which in turn leads to increased solubility of C in the matrix and partial dissolution of the prior formed carbides. c_p and c_{eq} in each phase are obtained using *ThermoCalc* Fe database, a thermodynamic calculation program (details of which are not shown here). Other parameters are obtained from the literature, including bulk diffusivity and activation energy of Cr [55, 58] and Mo [4, 59, 60] as well as the lattice parameter a_m of the matrix phase of F.C.C stainless steel [61].

Table 2. Parameters of 316H austenitic stainless steels used in the simulation of phase transformation

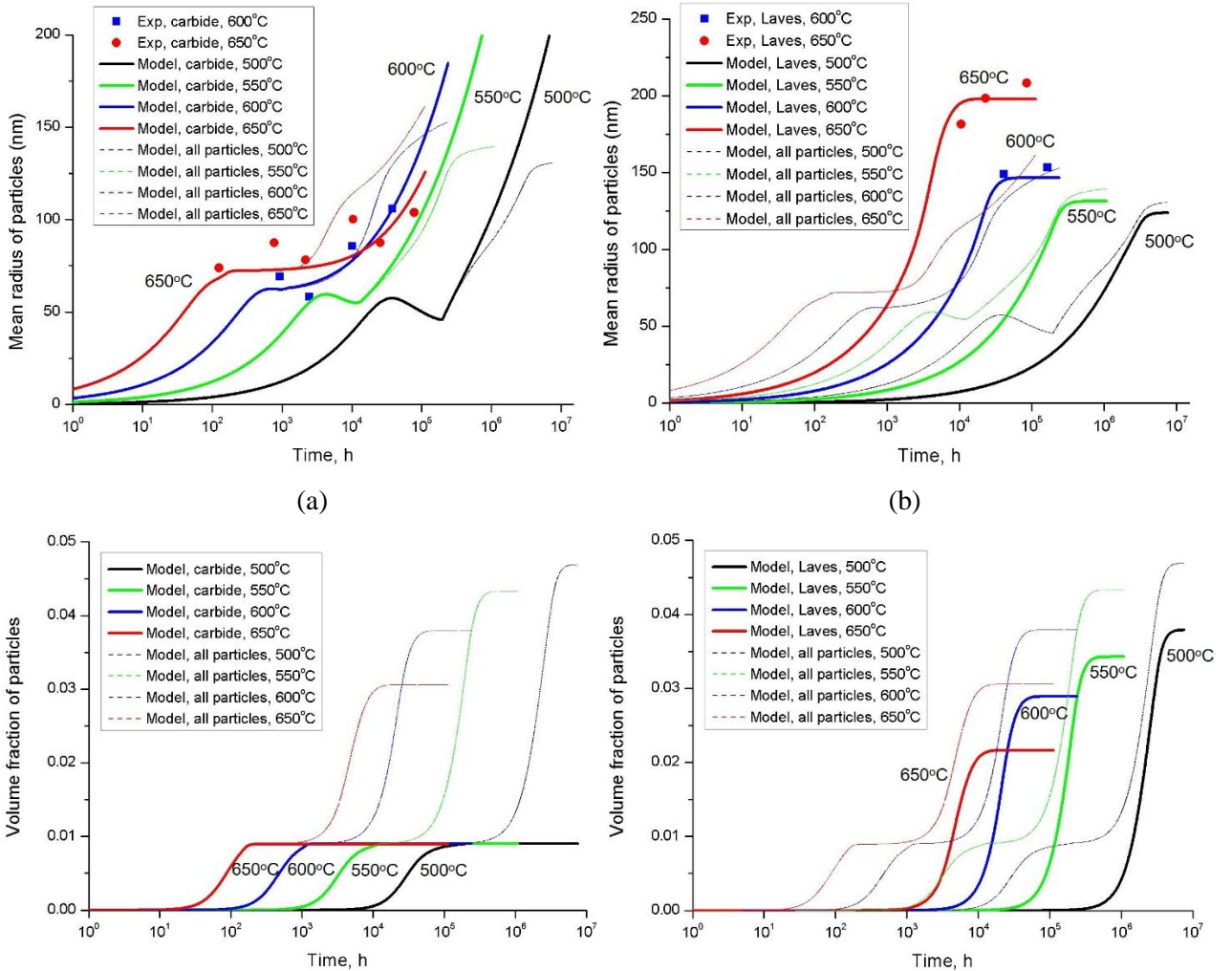
Parameter	Description	Unit	Phase or element	Value			
a_m	Lattice parameter for F.C.C. stainless steel	m		3.6×10^{-10}			
N_0	Nucleation site density	m^{-3}	Carbide	1×10^{13}			
			Laves	5×10^{14}			
V_m	Molar volume	$m^3 \text{ mol}^{-1}$	Carbide	6×10^{-6}			
			Laves	2×10^{-6}			
χ	Interfacial energy	$J \text{ m}^{-2}$	Carbide	0.3			
			Laves	0.25			
D_0	Bulk diffusion pre-exponential term	$m^2 \text{ s}^{-1}$	Cr	1.5×10^{-4}			
			Mo	7.4×10^{-4}			
Q_0	Bulk diffusion activation energy	$kJ \text{ mol}^{-1}$	Cr	240			
			Mo	283			
c_0	Initial concentration in the matrix	wt. %	Cr	16.25 (initial intergranular carbides deducted)			
			C	0.0375 (initial intergranular carbides deducted)			
			Mo	2.33			
c_p	Solute concentration in the precipitate	wt. %		500°C	550°C	600°C	650°C
			Cr in carbide	69.85	69.05	68.32	67.52
			C in carbide	5.13	5.13	5.13	5.13
			Mo in Laves	50	50	50	50
c_{eq}	Equilibrium concentration in the matrix	wt. %	Cr	15.64	15.69	15.75	15.83
			C	7.25×10^{-6}	2.92×10^{-5}	9.48×10^{-5}	2.97×10^{-4}
			Mo	0.25	0.46	0.76	1.16

C_f	Coarsening reduction factor	Carbide	1	1	0.3	0.03
-------	--------------------------------	---------	---	---	-----	------

4.1.2 Results and evaluations

The calculated evolutions of mean particle radius, volume fraction and number density of individual species and intra-carbide $Cr_{23}C_6$, Laves Fe_2Mo and a mix of all phases are shown in Fig. 6 over the range 500°C to 650°C, together with some available data. The results for the volume fraction (Fig. 6 c and d) match the trend shown in Fig. 5. Taking 650°C as an example, intragranular carbides becomes visible between 10-10² h, while Laves becomes visible between 10³-10⁴ h. At all tested temperatures, intragranular carbide precipitates are found to transform and saturate much faster, but with a much smaller maximum volume fraction than Laves phase. The evolution of the mean radius (Fig. 6a) and number density (Fig. 6e) of carbides clearly depicts the stages of fast growth, saturation and coarsening. The observed decrease of the mean radius at 550°C and 500°C (Fig. 6a) before coarsening is due to competition between a slow rate of growth and continuous nucleation of new nuclei towards saturation (Eq. 10). Over the considered time period at each temperature, no significant coarsening of Laves can be observed. The overall result (dashed line in Fig. 6) of all phases initially resembles that of carbides and gradually resembles that of Laves phase as the time is increased, indicating a switch of dominating phases in terms of population as the transformation proceeds. Another trend is observed such that the increase in temperature tends to give rise to fewer particles of larger mean size.

Figure 6 also demonstrates that an identical microstructural state at the service temperature may not be able to be reproduced in accelerated tests at higher temperatures.



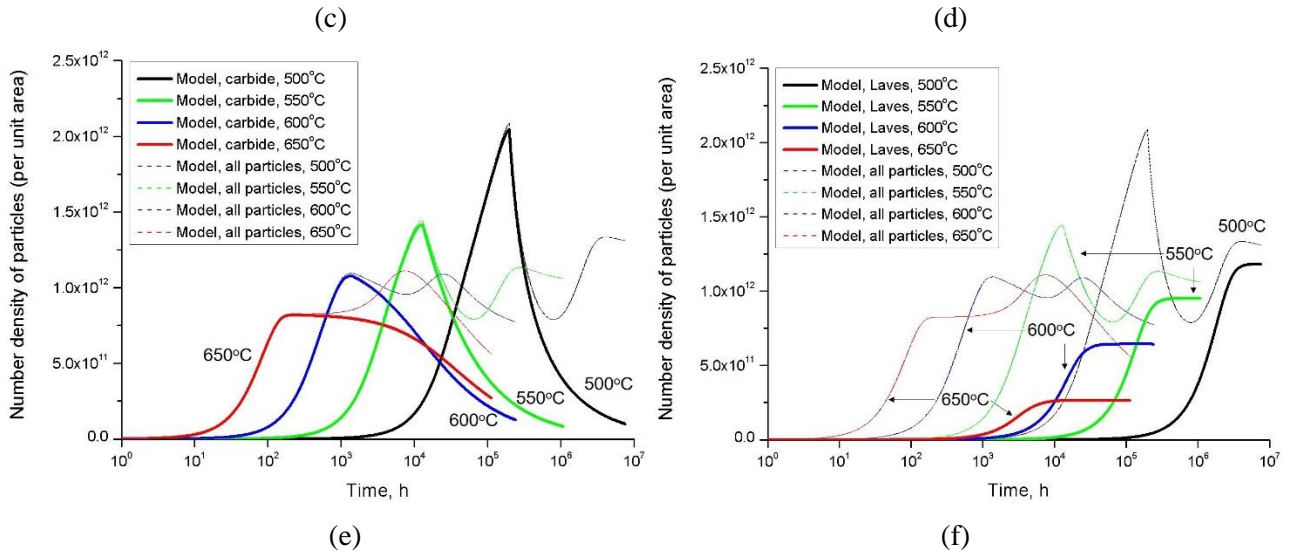
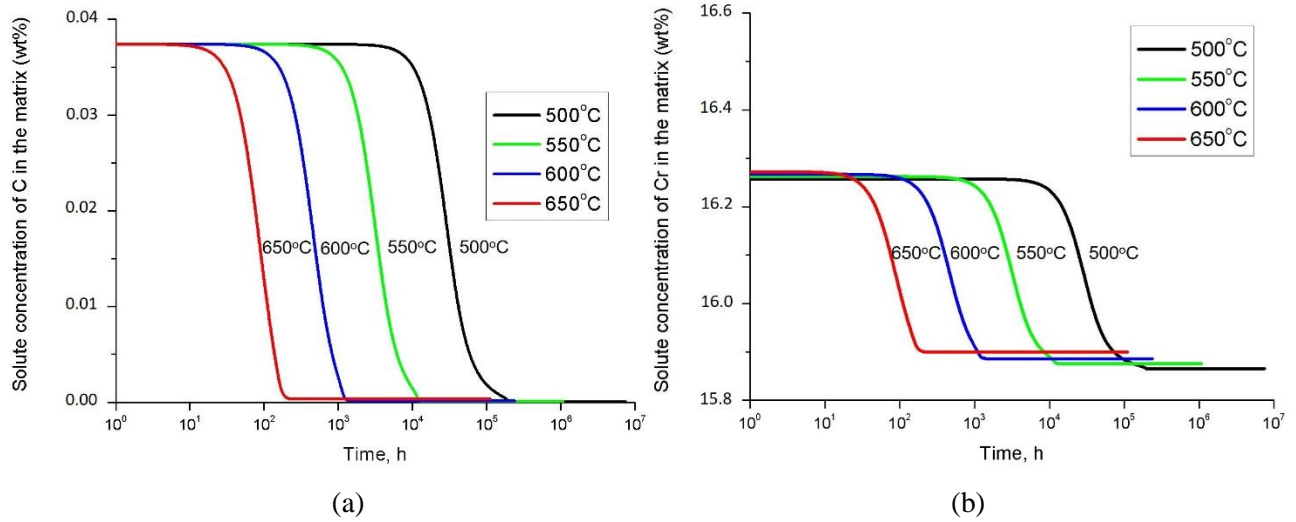


Figure 6. Evolution of the mean particle radius r_p (a and b), volume fraction f_v (c and d) and number density per unit area N_p (e and f) for intragranular carbide (solid lines in a, c and e) and Laves phase (solid lines in b, d and f), at temperatures from 500°C to 650°C. The overall results for all intragranular particles (dashed lines) are also shown in each figure.

Figure 7 presents the evolution of concentration of C , Cr and Mo in the matrix during phase transformation, which decreases towards the equilibrium value. Note that the equilibrium value of Mo differs significantly at different temperatures, as calculated by *ThermoCalc* (Table 2). This can be attributed to the large variation in the solubility of Mo in the matrix at different temperatures. Depletion of Cr is found to be relatively small compared with that of C and Mo . The saturation of each element accelerates as the temperature increases.



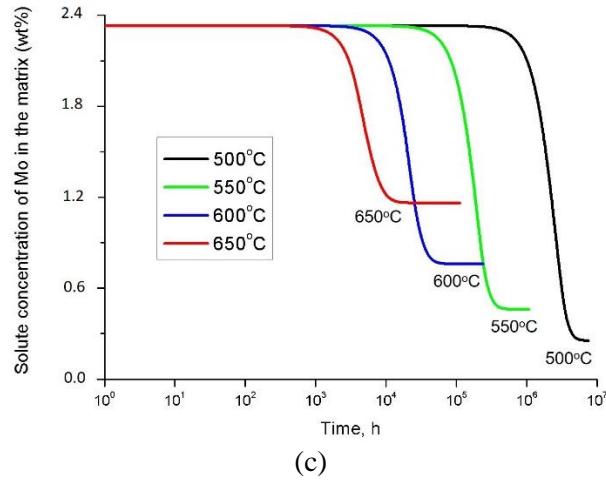


Figure 7. Evolution of concentration of (a) C , (b) Cr and (c) Mo in the matrix phase during thermal ageing at temperatures from 500°C to 650°C.

Figure 8 shows the mean spacing of all intra-particles as calculated from Eq. (4). The mean spacing decreases from infinity to a finite value as the transformation proceeds. However, simultaneous transformation of carbides and Laves phase with different kinetics is observed to complicate the evolution of mean spacing, exhibiting multiple minima, but eventually it increases after Laves phases have saturated.

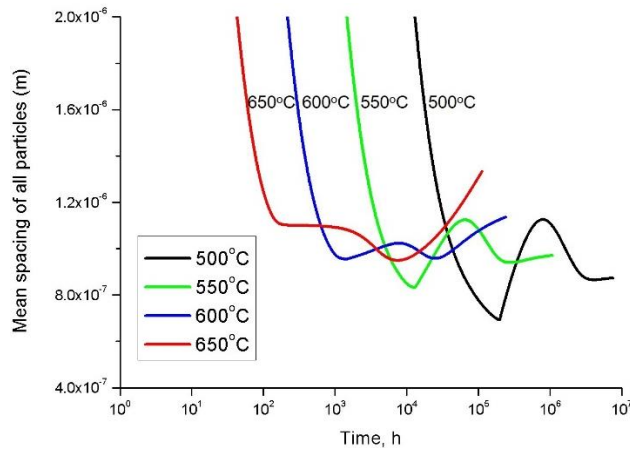


Figure 8. Evolution of mean spacing of all intra-particles at temperatures from 500°C to 650°C.

4.2 Evaluation of monotonic plastic deformation at different temperatures

Secondly, we evaluate the effect of thermal solute drag by simulating monotonic uniaxial tensile plastic deformation of initially solution treated (ST) 316H stainless steels from room temperature (RT) to 650°C. The recovery of dislocation structure and phase transformations are ignored in the considered temperature range during the short duration of the test.

In this simulation, the material is initially assumed to be free of residual stresses and the distribution of all microstructure elements are such that the CRSS is identical on all slip systems, i.e. with initially identical state variables (L_d , L_s , L_p) in Eq. (3), but the CRSS needs to be scaled when the temperature changes as the shear modulus varies with temperature [4, 21]. The simulation is stress controlled with different increments applied during elasticity and plasticity [16, 21]. Micro-yielding occurs when the initial value of the CRSS is achieved on the local slip systems, after which the plastic shear strain rate on the active slip systems is calculated by Eq. (1). At this stage, the increase of CRSS is only given by the evolution of L_d due to dislocation multiplication.

The values of most parameters in the model in this simulation (listed in Table 3) are the same as reported and validated in our previous work for both monotonic and creep deformation [16, 21, 22]. They were determined from geometric or physical requirements and describe the intrinsic deformation mechanisms that do not require a calibration process. Changes are made to two parameters: (1) the initial number of forest dislocation junctions per unit area (N_{do}) is reduced to $1 \times 10^{13} \text{ m}^{-2}$ for initially solution-treated 316H stainless steels, as measured by Morris and Harris [11]; (2) α_0 in the activation energy ΔF_0 in Eq. (1) is set to be 0.5, as used by Frost and Ashby [4], to simulate a weak combination of obstacles (forest dislocations + solid solution), where a value of 1 has been fitted and used in our previous work on ex-serviced plus laboratory aged materials with considerable precipitates.

For additional parameters associated with thermal solute drag (Eq. 2), Q_{sol} is considered to be equal to the activation energy for dislocation core diffusion [22, 62, 63]. ξ_{max} is modified from the value reported by Schmidt and Miller [62]. A and B are chosen to fit the monotonic tensile data of 316 stainless steels obtained by Schmidt and Miller [62], where the temperature-dependent constant A is positive only above 400°C. Asbury [64] has reported the solute complexes $Mo-C$ or $Mo-N$ to be responsible for the solute drag, thus c_s is simply taken here to be the concentration of Mo . In fact, it can be seen that, at 600°C and 650°C, the onset of Mo depletion in our simulated results (Fig. 7c) seems to coincide with the beginning of a creep rate increase, which then leads to the first secondary stage at relatively low stresses (Fig. 1).

Table 3. Material parameters of Type 316H austenitic stainless steel used in the simulation

Parameter	Value	Eq.	Ref.	Parameter	Value	Eq.	Ref.
b	$2.5 \times 10^{-10} \text{ m}$	(1)	[16]	D_c	$6.47 \times 10^{-15} \text{ m}^2/\text{s}$	(12)	[22]
$\dot{\gamma}_0$	1 s^{-1}	(1)	[22]	$\log(Z_{max})$	2.6	(2)	[62]
a_0	0.5	(1)	[3]	Q_{sol}	159 kJ mol^{-1}	(2)	[22]
a_d	0.35	(8)	[16]	c_s	0.0233	(2)	
a_p	0.84	(8)	[21, 65]	B	5	(2)	
a_s	0.000457	(8)	[21, 66]	A	10 (435°C) 12 (538°C)	(2)	
N_{do}	$1 \times 10^{13} \text{ m}^{-2}$	(9)	[11]		7 (600°C) 3 (650°C)		

Figure 9 compares the simulated monotonic tensile stresses normalized by temperature-dependent modulus with relevant experimental data at different strain levels up to 30%, from room temperature to 650°C. A further comparison is also shown in the figure by turning off the effect of solute drag throughout the simulation ($F_{sol} = 0$). A gradually pronounced peak can be observed in the stress-temperature data at an intermediate temperature range as more and more plastic strain accumulates. This is well captured by the model and the comparison clearly demonstrates the important role of solute drag on the mechanical behaviour of the solution treated (ST) 316H stainless steel.

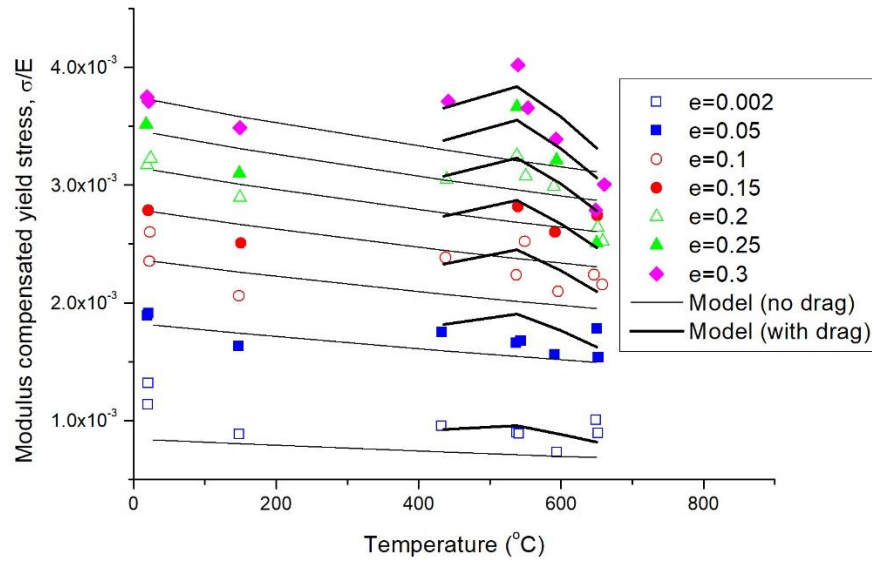


Figure 9. Comparison of simulated normalized stress of solution treated (ST) 316H across a range of temperatures at different strain levels, with and without consideration of the effect of solute drag.

4.3 Evaluation of multiple secondary stages during creep

Finally, this section evaluates the creep rate vs. time curves shown in Fig. 1, in particular, the phenomenon of multiple secondary stages. Here we select three curves of the specimens with designation AAL with three different stresses at 600°C and 650°C as shown in Fig. 1. However, taking into account the variability or scatter in the creep curves due to slight change in the chemical composition (Fig. 2), we intend to understand how, and to what extent, the evolution in the microstructural state can be correlated to the change in the creep properties of the material, but do not attempt to fit each particular curve.

In order to identify the dominant mechanism(s) for the multiple secondary stages, it is critical to understand the reason for the increase of creep rate after each secondary stage. Apart from the extensive damage accumulation (cavitation), which is usually dominant in the last tertiary stage and can cause significant increase in creep rate, we propose the following candidate thermal softening mechanism(s) based on the physics that have already been considered in the model:

- (i) Alternative competition between, or dominance of, hardening and recovery in determining the evolution of the dislocation structure;
- (ii) Complex evolution of the mean inter-particle spacing of the precipitates during phase transformation (Fig. 8);
- (iii) Reduced effect of thermal solute drag due to depletion of atoms in the solute clusters by phase transformation.

Here we examine these factors by undertaking a series of sensitivity studies. The extensive damage accumulation (cavitation), is not considered in the current model.

4.3.1 Creep without phase transformation

We start with mechanism (i) above by simulating creep without consideration of phase transformations. For simplicity, we take one stress at each temperature as an example. The initial ST material is first subjected to tensile pre-straining at each temperature up to the required stress, using the same procedure, assumptions and parameters as in the last section for monotonic plastic deformation. The material is then allowed to creep at constant load, during which the dislocation structure evolves by glide-controlled multiplication and climb-controlled recovery, as manifested by the change of the number of forest dislocation junctions at each time step. Phase transformations are ignored, i.e. the Orowan strength (Eq. 2) and micro-scale internal stress (Eq. 1) are both zero.

The simulated creep rate vs time curves are shown in Fig. 10. The solid and dashed curves represent the response without and with consideration of solute drag respectively, where the solute drag parameters for the dashed curve take the values shown in Table 2. These simulations produce standard creep curves such that the rate of recovery gradually catches up with the rate of hardening from the early stage of creep (primary) to the later stage (secondary), leading eventually to a dynamic balance. Without any phase transformations, the effect of solute drag is found only to be additional strengthening as reflected from the reduced creep rate. This is because the effect of solute drag becomes enhanced when the strain rate gradually catches up with the diffusion rate of solute elements during creep (i.e. ζ approaches the peak value ζ_{max} in Eq. 2). Despite this, the accumulation of strain and dislocations during tensile pre-straining when the required stress for creep is achieved is less pronounced compared with when solute drag is ignored (Fig. 9). The phenomenon of “multiple secondary stages” is not observed, indicating that the competition between dislocation hardening and recovery alone cannot explain the phenomenon.

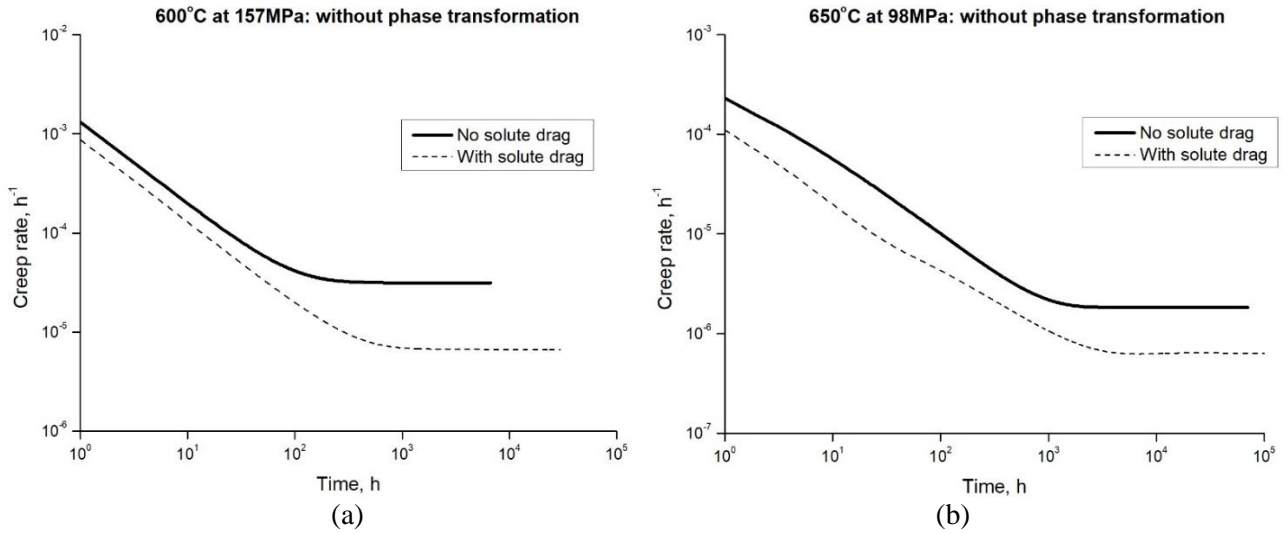


Figure 10. Predictions of creep rate vs time curves at (a) 600°C 157 MPa and (b) 650°C 98 MPa, without considering phase transformation.

4.3.2 Creep with phase transformations

We now take into account the interaction between phase transformations and creep with all mechanisms being active. Initially, we ignore the effect of solute drag (setting $F_{sol} = 0$), thus we examine mechanism (ii) described earlier. Then solute drag is taken into account. The simulation procedure is similar to that adopted in the last section, except that at each time step during creep, both intragranular carbides and Laves phases are allowed to transform, which leads to the development of the Orowan strength (τ_p) and the micro-scale internal stress upon loading [21, 34].

Additional parameters are needed to describe the effect of creep on these phase transformations. These are: (1) the change of the diffusivity of *Cr* and *Mo* with accumulation of dislocations (Eq. 14); (2) reduced activation energy for nucleation (Eq. 13). For (1), the bulk diffusivity of the two elements is shown in Table 2 while the dislocation core (pipe) diffusivity of the two elements in 316 stainless steels is found or estimated based on [4, 67] and is not shown here. The dislocation density in individual grains is updated at each time step based on the evolution of L_d . For (2), the acceleration parameter w is kept the same for both carbide and Laves phases, and two values are chosen for comparison, 1 and 0.1. Further, to be consistent and to avoid any numerical instabilities, an additional issue is addressed here, such that a_0 in ΔF_0 in Eq. (1) is kept to be the same constant value of 0.5 as in the last section, although it is understood that the microstructural state (population of precipitates) may gradually evolve and this may, in practice, influence the value of a_0 .

The updated creep rate vs time curves are shown in Fig. 11. The original curves in Fig. 10 are also included for comparison. In general, at both temperatures, in comparison with Fig. 10, precipitation gradually enhances the creep strength (reduced creep rate) of the material, which also depends on the value of the acceleration parameter (w) for the transformations employed in the simulations. The creep rate decreases faster as the nucleation rate becomes faster (w becomes smaller). Some minima or increase in creep rate can be seen, even when solute drag is ignored, which is a direct consequence of the complex evolution of the mean spacing (Fig. 8) or the corresponding Orowan strength. As the effect of solute drag stabilises, the creep rate starts to decrease again as a result of extensive dislocation multiplication (hardening). A new dynamic balance between hardening and recovery is yet to be achieved towards the second secondary stage. Compared with 650°C, a sharper increase in creep rate can be observed at 600°C after the first secondary stage when $w = 0.1$. This is when the growth of particles outweighs nucleation (Eq. 10), thus reducing the precipitate strengthening, and coincidentally, when Mo in the matrix starts to be depleted (onset of Laves precipitation, Fig. 7c), thus weakening the effect of solute drag. Such a trend does not occur at 650°C when $w = 0.1$ because the precipitation kinetics are different. The curves then appear to be much smoother. It is further noted that the stabilisation at 600°C takes a longer time than that at 650°C, resulting in a more pronounced enhancement in creep rate at 600°C. This can be attributed to the slower depletion of Mo at 600°C to a lower equilibrium value compared with that at 650°C (Fig. 7c).

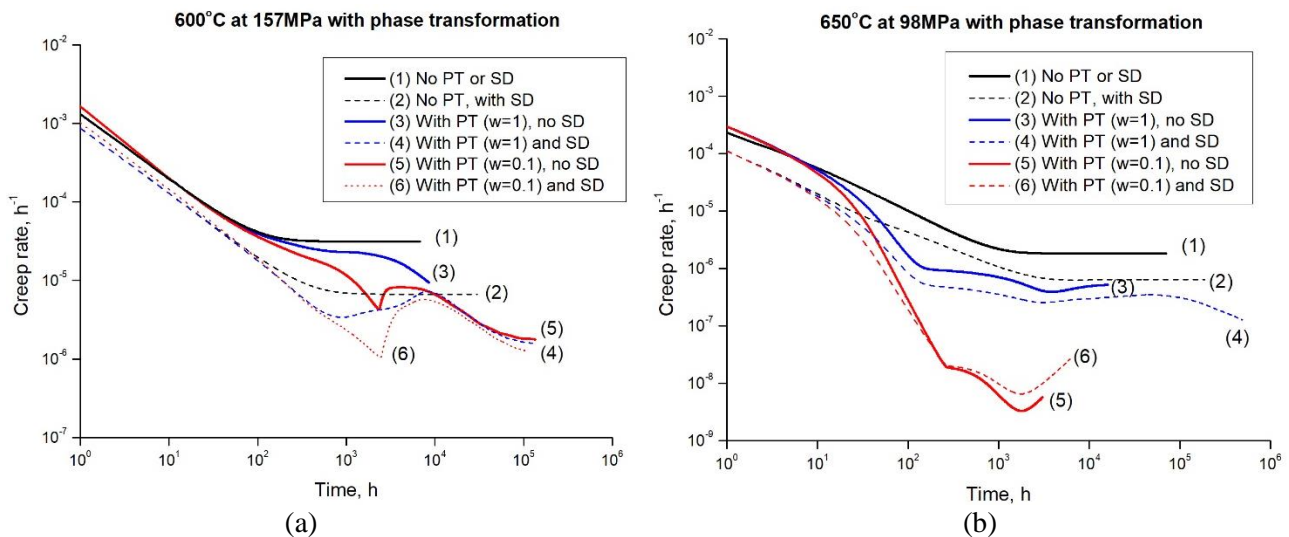


Figure 11. Predictions of creep rate vs time curves at (a) 600°C 157 MPa and (b) 650°C 98 MPa, taking into account the creep-affected phase transformation. PT: phase transformation; SD: solute drag.

4.3.3 Refinement of creep curves

In Fig. 11, a reduction of the acceleration parameter w is found to have a more pronounced effect at 650°C compared with that at 600°C. This can be attributed to an enhancement of the athermal Orowan bowing process triggered by faster precipitation at 650°C of a large number of small particles nucleated early in the process. In reality, at relatively low applied stress levels at elevated temperatures, some portions of the dislocations may climb over and bypass the precipitates [14], as mentioned earlier, thus the Orowan bowing process can be inhibited. In addition, not all precipitates are strong, i.e. some small particles can be easily cut by dislocations, thus the strengthening is much weaker than the Orowan bypassing mechanism [13, 68]. Both factors would lead to a reduced precipitate strengthening. Evidence of this can be found in the strengthening-mechanism map of 316 stainless steels proposed by Aplin and D'Angelo [13], where the creep mechanism, particularly around 650°C at similar low stress levels to that considered here is termed “viscous glide”, an indication of weak precipitation strengthening.

Here we propose a simple refinement of the prediction to take this into account by neglecting the Orowan strength ($\tau_p = 0$) throughout the simulation at each temperature, but retaining the depletion of

solute elements as the sole effect of phase transformation. The updated creep rate vs time curves are shown in Fig. 12, taking a single value of $w = 0.1$. Without Orowan strengthening, the creep rate (No. (4) in Fig. 12) significantly increases, particularly at 650°C. The curves become closer to those in the absence of any phase transformations, except for the subsequent increase of creep rate, which is caused purely by the reduced effect of solute drag.

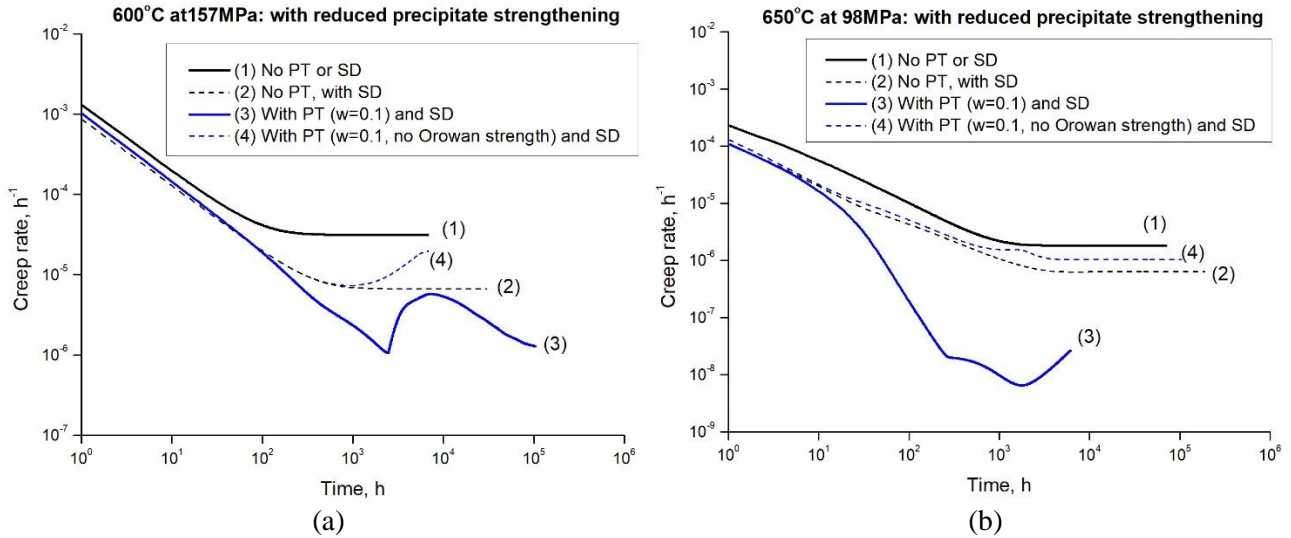


Figure 12. Comparison of creep rate vs time curves at (a) 600°C 157 MPa and (b) 650°C 98 MPa with/without reduced precipitate strengthening (no Orowan strength), taking a single value of $w = 0.1$. PT: phase transformation; SD: solute drag.

Finally, having considered different deformation mechanisms, the proposed model is used to simulate the creep behaviour of solution treated 316H stainless steel at 600°C and 650°C and the simulations are compared with the experimental data shown in Fig. 1. Three stresses are selected at each temperature for the comparison, which is demonstrated in Fig. 13. The tertiary stage has been partly truncated as no damage mechanisms have been considered in the model. The acceleration parameter w is taken to be 0.1 for both temperatures. Note the Orowan strength at 650°C is ignored at all the considered stresses. The model provides good agreement with the data, well within the variability as shown in Fig. 2. Some discrepancies are discussed below.

At 600°C, the model has predicted the earlier achievement of the secondary stage (at 108 MPa and 157 MPa) and a lower minimum creep rate at 108 MPa compared with data. Some dislocation climb-controlled precipitate bypassing may have been operative at these relatively low stresses, as mentioned earlier, which can reduce precipitate strengthening and alter its dependency on particle size and mean spacing. At these low stresses, the model predicts a sharp increase in creep rate after the achievement of the secondary stage, which also seems to be reflected in the data. This, as explained earlier, can be attributed to the simultaneous precipitate strengthening reduction and thermal solute drag weakening. The model further shows that the creep rate continues to decrease towards the second minimum and a second steady state is yet to be achieved beyond the experimental creep rupture life at each of these stresses. This indicates that, in practice, on one hand, “multiple secondary stages” may not occur at this temperature because damage accumulation would appear earlier than the achievement of the second steady state. On the other hand, the early tertiary stage at this temperature may be a consequence of the microstructure evolution considered in this work rather than significant damage accumulation.

At 650°C, the model captures the “multiple secondary stages”, although less pronounced than the data. The predicted lower creep rates may be further compensated by reducing the solute bypassing strength (τ_s in Eq. 9) since solute atoms may become mobile and diffuse rapidly at this temperature thus contributing less to the strength than at 600°C. Earlier damage accumulation may also be responsible for the more pronounced discrepancy when the applied stress becomes higher. Compared with 600°C, the sharp increase in creep rate does not occur either in the data or in the model prediction

due to the different kinetics in precipitation process as mentioned earlier. The predicted achievement of the second steady state within the life span shown in the data indicates that the “multiple secondary stages” phenomenon is more likely to occur at 650°C.

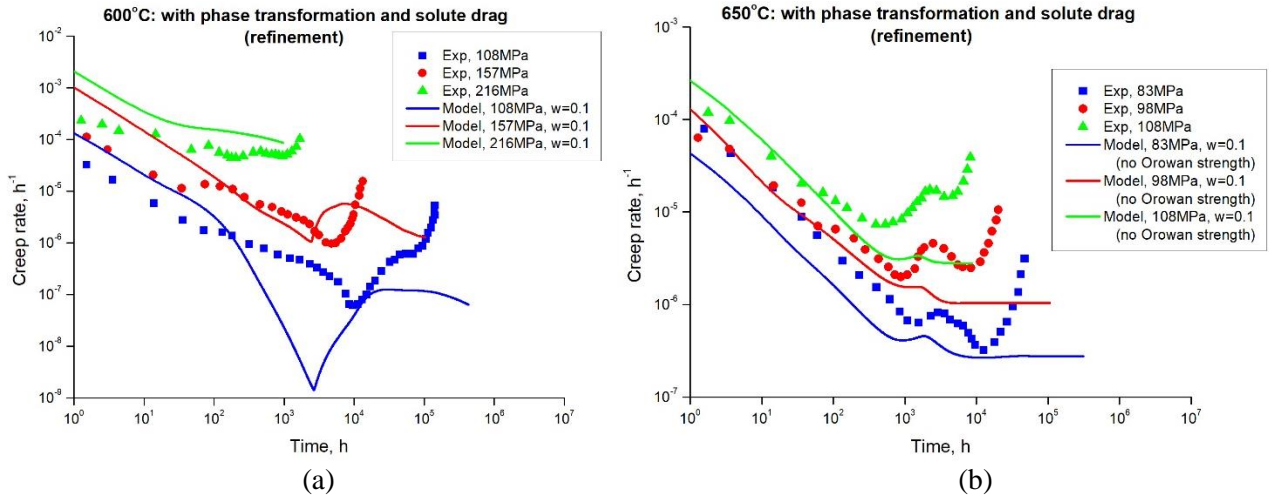


Figure 13. Refined predictions of creep rate vs time curves at (a) 600°C and (b) 650°C, taking into account both effect of solute drag and phase transformation but neglecting the Orowan strength described in Eq. 8. Solid data points represent experimental data and solid lines represent model predictions.

The corresponding creep curves at 600°C and 650°C are presented in Fig. 14, with the experimental curves transformed from the creep rate data in Fig. 13. At 600°C, it clearly shows that the interaction between solute drag and phase transformation can contribute to the tertiary stage. At 650°C, the “multiple secondary stages” phenomenon appears less pronounced compared with the plot of creep rate vs time curves (Fig. 13b). However, understanding the effect of solute drag and phase transformation on the creep behaviour at elevated temperatures is beneficial to the assessment of the evolution of a material’s internal state and future model development of damage accumulation.

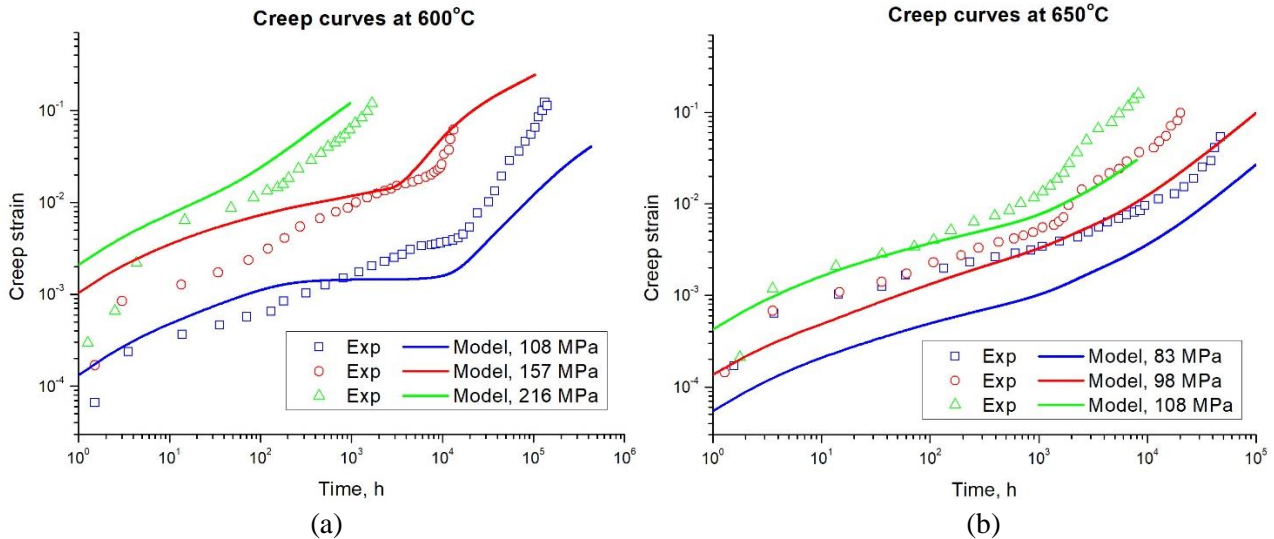


Figure 14. Comparison of creep curves at (a) 600°C and (b) 650°C at the corresponding stresses considered in Fig. 13. Solid data points represent experimental data and solid lines represent model predictions. The experimental creep curves were transformed from the reported creep rate vs time curves in Fig. 13.

5. Conclusion

Physically understanding the internal mechanisms of creep in nuclear power plant materials, such as 316H stainless steels, during complex thermo-mechanical loading histories, is vital to the realistic

life assessment of critical engineering components. The initially solution-treated (ST) 316H stainless steels are thermodynamically unstable - different phases can transform from the supersaturated solid solution in service, which can then influence the creep behaviour of the material. In this paper correlation between the change of creep properties and the evolution of microstructural state of the material has been mechanistically established by a multiscale self-consistent model, incorporating the extended JMAK phase transformation model and a thermal solute drag model.

The integrated model has been applied to evaluate the creep behaviour of ST 316H stainless steels at 600°C and 650°C, with the main focus on the phenomenon and mechanism of “multiple secondary stages” observed in the creep rate vs time response. This has been attributed to the combined effect of thermal solute drag and phase transformation on dislocation motion, multiplication and recovery. Solute drag plays an important role such that it either enhances the creep strength as the creep rate decreases, or reduces the creep strength when its effect is attenuated by the depletion of the controlling solute species *Mo* by the phase transformation process. Evolution of the microstructural state may also change the deformation kinetics and break the dynamic balance between hardening and recovery, resulting in a transient response until a new balance is achieved towards a new steady state.

It is further noted that care should be taken when considering the effect of phase transformations on creep since other mechanisms or interactions may occur such as dislocation-climb bypassing or dislocation-glide cutting of small precipitates, both of which would reduce the strengthening effect of the precipitates. Consideration of the detailed phase composition may be necessary as it could affect the degree of solute drag and the details of the phase transformation process. A more detailed study on precipitation is needed to investigate this in depth. Damage accumulation in the form of grain-boundary cavitation is yet to be incorporated, which would further improve the matching with data. Finally, understanding the effect of thermal solute drag and phase transformation on the creep behaviour at elevated temperatures is beneficial to the assessment of the evolution of a material's internal state and enables physical deformation modelling for a broader range of complex problems in the future, such as stress relaxation and elastic follow-up [69].

Acknowledgements

The authors are grateful to EDF Energy Ltd for the financial support of the research described in this paper.

Data Availability

The data used in this paper can all be found in the respective references.

References

- [1] Murty KL, Charit I. Structural materials for Gen-IV nuclear reactors: Challenges and opportunities. *Journal of Nuclear Materials*. 2008;383:189-95.
- [2] Spindler M. Discussion document-Creep constitutive models for type 316H. British Energy. 2010.
- [3] Hu JN. A theoretical study of creep deformation mechanisms of Type 316H stainless steel at elevated temperatures. DPhil Thesis, University of Oxford. 2015.
- [4] Frost HJ, Ashby MF. Deformation-mechanism maps : the plasticity and creep of metals and ceramics. Oxford: Pergamon Press; 1982.
- [5] Penny RK, Marriott DL. Design for creep. 2nd ed ed. London: Chapman & Hall; 1995.
- [6] Dyson B. An alternative constitutive description of AISI 316 stainless steel for use in weld reheat cracking. Report prepared for Nuclear Electric plc Barnwood Gloucester. 1997.
- [7] Chen B, Smith DJ, Flewitt PEJ, Spindler MW. Constitutive equations that describe creep stress relaxation for 316H stainless steel at 550 degrees C. *Mater High Temp*. 2011;28:155-64.

- [8] Schmidt CG, Miller AK. A Unified Phenomenological Model for Non-Elastic Deformation of Type-316 Stainless-Steel .1. Development of the Model and Calculation of the Material Constants. *Res Mechanica*. 1981;3:109-29.
- [9] Kubo K, Ohba T, Kimura K, Abe F, Yagi K. Effect of changes in microstructure on complex creep deformation behaviour of SUS 316. *CAMP-ISIJ*. 1994;7:1791-.
- [10] Kubo K, Ohba T, Kimura K, Abe F, Yagi K, Irie H. Effect of microstructural evolution on complex creep deformation behaviour of SUS 316 steel at 823K and 923K. *CAMP-ISIJ*. 1996;9:1435-.
- [11] Morris DG, Harries DR. Creep and rupture in Type 316 stainless steel at temperatures between 525 and 900C-Part 1: creep rate. *Metal Science*. 1978:525-31.
- [12] National Institute of Materials Science N. Micrographs and Microstructural Characteristics of Crept Specimens of 18Cr-12Ni-Mo Stainless steel for Boiler and Heat exchanger seamless tubes (SUS 316H TB). 2003.
- [13] Aplin PF, Angelo DD. Dislocation-creep mechanisms in type 316 steel. . In *Creep and Fracture of Engineering Materials and Structures*, eds B Wilshire, RW Evans Institute of Metals, London. 1990:537-45.
- [14] Mclean M. On the Threshold Stress for Dislocation Creep in Particle Strengthened Alloys. *Acta Metallurgica*. 1985;33:545-56.
- [15] Chen B, Flewitt PEJ, Smith DJ, Cocks ACF. A review of the changes of internal state related to high temperature creep of polycrystalline metals and alloys. *International Materials Reviews*. 2015;60:1-29.
- [16] Hu JN, Cocks ACF. A multi-scale self-consistent model describing the lattice deformation in austenitic stainless steels. *International Journal of Solids and Structures*. 2016;78-79:21-37.
- [17] Li DF, O'Dowd NP. On the evolution of lattice deformation in austenitic stainless steels-The role of work hardening at finite strains. *Journal of the Mechanics and Physics of Solids*. 2011;59:2421-41.
- [18] Clausen B, Lorentzen T, Leffers T. Self-consistent modelling of the plastic deformation of FCC polycrystals and its implications for diffraction measurements of internal stresses. *Acta Materialia*. 1998;46:3087-98.
- [19] Neil CJ, Wollmershauser JA, Clausen B, Tome CN, Agnew SR. Modeling lattice strain evolution at finite strains and experimental verification for copper and stainless steel using in situ neutron diffraction. *International Journal of Plasticity*. 2010;26:1772-91.
- [20] Wang H, Clausen B, Tome CN, Wu PD. Studying the effect of stress relaxation and creep on lattice strain evolution of stainless steel under tension. *Acta Materialia*. 2013;61:1179-88.
- [21] Hu JN, Chen B, Smith DJ, Flewitt PEJ, Cocks ACF. On the evaluation of the Bauschinger effect in an austenitic stainless steel—The role of multi-scale residual stresses. *International Journal of Plasticity*. 2016;84:203-23.
- [22] Hu JN, Cocks ACF. Effect of creep on the Bauschinger effect in a polycrystalline austenitic stainless steel. *Scripta Mater*. 2017;128:100-4.
- [23] Robson JD, Bhadeshia HKDH. Modelling precipitation sequences in power plant steels .1. Kinetic theory. *Materials Science and Technology*. 1997;13:631-9.
- [24] Perez M, Dumont M, Acevedo-Reyes D. Implementation of classical nucleation and growth theories for precipitation. *Acta Materialia*. 2008;56:2119-32.
- [25] Deschamps A, Brechet Y. Influence of predeformation and ageing of an Al-Zn-Mg alloy - II. Modeling of precipitation kinetics and yield stress. *Acta Materialia*. 1998;47:293-305.
- [26] Eshelby JD. The determination of the elastic field of an ellipsoidal inclusion and related problems. *Proc R Soc Lond A* 1957;241:376-96.
- [27] Mura T. *Micromechanics of defects in solids*. The Hague ; London: Martinus Nijhoff; 1982.
- [28] Kroner E. On the Plastic Deformation of Polycrystals. *Acta Metallurgica*. 1961;9:155-61.
- [29] Budiansky B, Wu TT. Theoretical prediction of plastic strains of polycrystals. *Proc 4th Congr Appl Mech*. 1962:1175-85.
- [30] Asaro RJ, Needleman A. Overview .42. Texture Development and Strain-Hardening in Rate Dependent Polycrystals. *Acta Metallurgica*. 1985;33:923-53.

- [31] Kocks UF, Mecking H. Physics and phenomenology of strain hardening: the FCC case. . Progress in Materials Science. 2003;48:171-273.
- [32] Henshall GA, Miller AK. Simplifications and Improvements in Unified Constitutive-Equations for Creep and Plasticity .1. Equations Development. Acta Metallurgica Et Materialia. 1990;38:2101-15.
- [33] Hu JN, Chen B, Smith DJ, Flewitt PEJ, Cocks ACF. Self-consistent modelling and the evaluation of lattice deformation in a polycrystalline austenitic stainless steel. Materials Today: Proceedings. 2015;2:S424-S33.
- [34] Ashby MF. Work Hardening of Dispersion-Hardened Crystals. Philosophical Magazine. 1966;14:1157-&.
- [35] Basoalto H, Dyson B. Predicting stress relaxation & LCF using a microstructure-based constitutive model. British Energy plc Contract Reference No 40072908 (SW19/02) 2003.
- [36] Dong Y, Nogaret T, Curtin WA. Scaling of Dislocation Strengthening by Multiple Obstacle Types. Metallurgical and Materials Transactions a-Physical Metallurgy and Materials Science. 2010;41A:1954-60.
- [37] Hu J, Cocks ACF. Correlation between microstructure evolution and creep properties of polycrystalline austenitic stainless steel. Proceedings of 23rd Structural Mechanics in Reactor Technology (SMiRT). 2015.
- [38] Friedel J. Dislocations. Reprinted with corrections ed. Oxford, Reading, Mass: Pergamon; [Distributed in USA by] Addison-Wesley Pub. Co; 1964.
- [39] Argon AS. Strengthening mechanisms in crystal plasticity. Oxford: Oxford University Press; 2008.
- [40] Shewmon PG. Transformations in metals. New York ; London: McGraw-Hill; 1969.
- [41] Christian JW. The theory of transformations in metals and alloys : an advanced textbook in physical metallurgy. 2nd ed. Oxford: Pergamon; 1975.
- [42] Yin YF, Faulkner RG. Simulations of precipitation in ferritic steels. Materials Science and Technology. 2003;19:91-8.
- [43] Zener C. Theory of Growth of Spherical Precipitates from Solid Solution. Journal of Applied Physics. 1949;20:950-3.
- [44] Baldan A. Review Progress in Ostwald ripening theories and their applications to nickel-base superalloys - Part I: Ostwald ripening theories. Journal of Materials Science. 2002;37:2171-202.
- [45] Morris DG, Harries DR. Creep and rupture in Type 316 stainless steel at temperatures between 525 and 900oC Part III: Precipitation behaviour Metal Science. 1978:542-9.
- [46] Perrard F, Deschamps A, Maugis P. Modelling the precipitation of NbC on dislocations in alpha-Fe. Acta Materialia. 2007;55:1255-66.
- [47] Embury JD, Deschamps A, Brechet Y. The interaction of plasticity and diffusion controlled precipitation reactions. Scripta Mater. 2003;49:927-32.
- [48] Burton B. The Influence of Solute Drag on Dislocation Creep. Philosophical Magazine a-Physics of Condensed Matter Structure Defects and Mechanical Properties. 1982;46:607-16.
- [49] Hirth JP, Lothe J. Theory of Dislocations. New York: John Wiley; 1982.
- [50] Pham MS, Iadicola M, Creuziger A, Hu L, Rollett AD. Thermally-activated constitutive model including dislocation interactions, aging and recovery for strain path dependence of solid solution strengthened alloys: Application to AA5754-0. International Journal of Plasticity. 2015;75:226-43.
- [51] Chen B, Flewitt PEJ, Smith DJ, Jones CP. An improved method to identify grain boundary creep cavitation in 316H austenitic stainless steel. Ultramicroscopy. 2011;111:309-13.
- [52] Faulkner RG. Microstructural examination of ex-Heysham header creep specimens. Internal report to EDF Energy. 2002.
- [53] Marshall P. Austenitic stainless steels : microstructure and mechanical properties. London: Elsevier Applied Science; 1984.
- [54] Feng Z. Microstructural evolution in austenitic stainless steels for extended life power station application. PhD Thesis for Loughborough University. 2011.

- [55] Fujita N, Bhadeshia HKDH. Modelling simultaneous alloy carbide sequence in power plant steels. *Isij International*. 2002;42:760-9.
- [56] Robson JD, Bhadeshia HKDH. Modelling precipitation sequences in power plant steels .2. Application of kinetic theory. *Materials Science and Technology*. 1997;13:640-4.
- [57] Chen Q, Jeppsson J, Agren J. Analytical treatment of diffusion during precipitate growth in multicomponent systems. *Acta Materialia*. 2008;56:1890-6.
- [58] Sourmail T. Precipitation in creep resistant austenitic stainless steels. *Materials Science and Technology*. 2001;17:1-14.
- [59] Nitta H, Yamamoto T, Kanno R, Takasawa K, Iida T, Yamazaki Y, et al. Diffusion of molybdenum in alpha-iron. *Acta Materialia*. 2002;50:4117-25.
- [60] Anderson TD, Perricone MJ, DuPont JN, Marder AR. The influence of molybdenum on stainless steel weld microstructures. *Welding Journal*. 2007;86:281s-92s.
- [61] Boeuf A, Crico S, Caciuffo R, Rustichelli F, Pomot I, Uny G. Effects of M23c6 Precipitation on the Lattice-Parameter of Aisi-304 Stainless-Steel. *Materials Letters*. 1985;3:115-8.
- [62] Schmidt CG, Miller AK. A Unified Phenomenological Model for Non-Elastic Deformation of Type-316 Stainless-Steel .2. Fitting and Predictive Capabilities. *Res Mechanica*. 1981;3:175-93.
- [63] Henshall A. Solute-enhanced back stresses and their role in a simplified phenomenological constitutive model for the nonelastic deformation of metals and alloys. Dissertation for Stanford Univeristy. 1987.
- [64] Asbury FE. Factors Influencing Long-Term Creep of Type-316 Steel at 600-Degrees-C. *Materials Science and Technology*. 1986;2:1123-30.
- [65] Foreman AJE, Makin MJ. Dislocation Movement through Random Arrays of Obstacles. *Philosophical Magazine*. 1966;14:911-24.
- [66] Hirth JP, Lothe J. Theory of dislocations. 2nd ed. Malabar, Fla: Krieger Publishing Co; 1992.
- [67] Smith AF. The diffusion of chromium in type 316 stainless steel. *Metal Sci*. 1975;9:375-8.
- [68] Gladman T. The physical metallurgy of microalloyed steels. London: Institute of Materials; 1997.
- [69] Wang YQ, Spindler MW, Truman CE, Smith DJ. Critical analysis of the prediction of stress relaxation from forward creep of Type 316H austenitic stainless steel. *Mater Design*. 2016;95:656-68.